JOURNAL OF AIRCRAFT
Vol. 31, No. 1, Jan.–Feb. 1994

Calculations of Hot Gas Ingestion for a STOVL Aircraft Model

D. M. Fricker* and J. D. Holdeman†
NASA Lewis Research Center, Cleveland, Ohio 44135
and
S. P. Vanka‡
University of Illinois at Urbana—Champaign, Urbana, Illinois 61801

Hot gas ingestion problems for STOVL (short take-off, vertical landing) aircraft are typically approached with empirical methods and experience. In this study, the hot gas environment around a STOVL aircraft was modeled as multiple jets in crossflow with inlet suction. The flowfield was calculated with a Navier-Stokes, Reynolds-averaged, turbulent, three-dimensional CFD code using a multigrid technique. A simple model of a STOVL aircraft with four choked jets at 1000 K was studied at various heights, head wind speeds, and thrust splay angles in a modest parametric study. Scientific visualization of the computed flowfield shows a pair of vortices in front of the inlet.

Nomenclature

D_j = characteristic length of jet nozzles, 0.0366 m (1.44 in.)
H = distance from ground to bottom of the aircraft (aircraft altitude or height)
k = turbulent kinetic energy
U_∞ = head wind velocity
V_j = jet nozzle exit velocity, 633 m/s (2080 ft/s)
x = axial Cartesian coordinate, zero at upstream boundary
x-y = vertical plane aligned in axial direction
x-z = horizontal plane
y = vertical Cartesian coordinate, zero at ground plane
y-z = vertical plane aligned in spanwise direction
z = spanwise Cartesian coordinate, zero at aircraft centerline plane
δ = thrust splay angle measured from the downward vertical toward symmetry plane
ε = turbulent energy dissipation

Introduction

HOT gas ingestion can cause significant problems for a STOVL (short take-off, vertical landing) aircraft, including reduced thrust and compressor stalls. These problems involve many hazards for the pilots, including very hard landings. During the design of a STOVL aircraft, hot gas ingestion problems are typically approached with empirical methods and experience.[1,2] Given the power of today's supercomputers and workstations, numerical methods employing efficient algorithms are becoming a viable engineering tool for analysis and design. In a previous endeavor, VanOverbeke and Holdeman[3,4] demonstrated the feasibility of CFD analysis for hot gas ingestion. This study is a follow-on effort exploring the practicality of using an efficient numerical method for the problem of hot gas ingestion.

Presented as Paper 92-0385 at the AIAA 30th Aerospace Sciences Meeting and Exhibit, Reno, NV, Jan. 6–9, 1992; received March 27, 1992; revision received Sept. 30, 1992; accepted for publication Oct. 25, 1992.

*Aerospace Engineer, Vehicle Propulsion Directorate, Army Research Laboratory (AMSRL-VP), M/S 5-11. Member AIAA.
†Senior Research Engineer, Internal Fluid Mechanics Division, MC 244. Associate Fellow AIAA.
‡Associate Professor, Department of Mechanical and Industrial Engineering. Member AIAA.

Flowfield Description

Ingestion of hot gases generates problems in two ways: 1) an average temperature rise results in a loss of engine thrust, and 2) a temperature distortion may cause the engine to stall. Engine exhaust gases may be ingested by far-field and/or near-field mechanisms. A schematic of these mechanisms is shown in Fig. 1.

The far-field mechanism results from the exhaust gases impinging on the ground and forming radial wall jets which flow forward, separate, and mix with the head wind. Near-field ingestion occurs with multiple jet configurations. Wall jets flowing out from the lift jets meet and create an upflow or fountain. This fountain flow can impinge on the aircraft's underside, flow along the fuselage to the engine inlets, and be ingested. The gases ingested by this near-field mechanism tend to be hotter, giving greater temperature distortion than those ingested by the far-field mechanism.

As stated earlier, the hot gas environment around a STOVL aircraft was modeled as multiple jets in crossflow with inlet suction. Mass sources represent the nozzle exits, and a mass

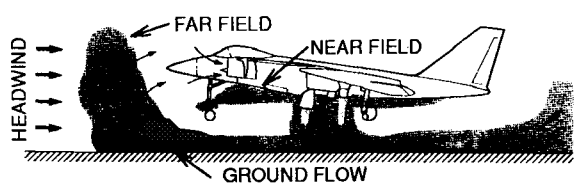

Fig. 1 Hot gas ingestion mechanisms.

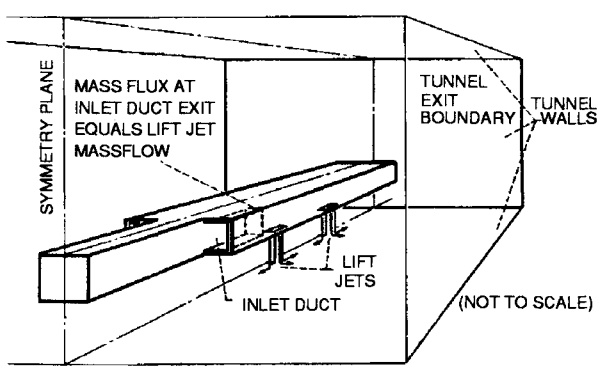

Fig. 2 STOVL Aircraft model.

sink at the end of the inlet provides the suction. The mass injected by the nozzles balances the mass removed by the inlet suction. This configuration is derived from the previous study by VanOverbeke and Holdeman.[3,4] To meet the requirements of the CFD code, the aircraft model is placed in a confined flow, i.e., a "wind tunnel." (It should be noted that changes in the width of the confinement did not significantly affect the flowfield in the vicinity of the jets and inlet for the same inflow and jet conditions. Thus, the wind-tunnel walls had minimal effect on the desired results.) Also, the aircraft model has no angle of attack due to the use of a Cartesian grid-based flow solver.

The STOVL aircraft model (see Fig. 2) is composed of rectangular solids for the fuselage and engine. For computational simplicity, the nose and the tail of the aircraft reach to infinity, and the model lacks wings. Baffles on the sides of the fuselage comprise the walls of the inlet. The nozzles are square in cross section and are flush with the bottom of the aircraft. The square cross section of the jets and the rectangular aircraft body result from the use of the Cartesian grid.

The four choked nozzles inject air at 1000 K (1340°F) straight down into the flowfield with a velocity of 633 m/s (2080 ft/s). Each lift jet issues from the nozzle exit in a uniform flow. The head wind is also a uniform flow, but at a temperature of 300 K (81°F). This approximates an aircraft landing with a forward speed, or an aircraft facing into a wind which lacks a boundary layer. In the baseline case, the head wind (U_∞) flows at 3% of the jet velocity (V_j), or about 19 m/s (37 kt), and the distance from the ground to the bottom of the aircraft model (H) is four times the characteristic length of the nozzles ($4D_j$). The parametric studies include: various altitudes ($H = 2–32D_j$) at a constant head wind ($U_\infty = 0.03V_j$); various head wind speeds ($U_\infty = 0.01–0.09V_j$) for a constant aircraft altitude ($H = 4D_j$); and various thrust splay angles ($\delta = 0–45$ deg) for a constant height ($H = 4D_j$) and head wind speed ($U_\infty = 0.03V_j$).

The physical dimensions of the aircraft model are given in Table 1. Note that the forward and aft nozzles have the same side-to-side separation, i.e., they are in-line, not offset.

Table 1 STOVL Aircraft model dimensions

Fuselage	
Width (nose)	$2.25D_j$
Width (tail)	$5.05D_j$
Height	$2.5D_j$
Length	∞
Inlet	
Width	$1.4D_j$
Height	$2.5D_j$
Length	$9.5D_j$
Jets separation	
Center-to-center	
Side-to-side	$3.25D_j$
Fore and aft	$6.0D_j$

Numerical Description

Calculation Domain

The grid geometry used for the baseline case is shown in Fig. 3. Exhibited are the centerline plane, the ground plane, and a vertical spanwise plane at the end of the domain as well as the aircraft model. The grid shows the high density of the calculation nodes in the region of the jets. For all calculations, symmetry assumptions allowed calculating only half of the physical domain.

The other boundary conditions for the calculation domain include an inflow simulating the head wind for the domain face in front of the aircraft model and an outflow condition for the domain face behind the model. All flow properties are defined for the inflow condition. The outflow condition, in contrast, merely assumes the properties of the axially nearest cells. The top, bottom, and remaining side of the domain are no-slip, stationary walls, as are the aircraft surfaces. All the walls assume adiabatic conditions for the energy equation. The symmetry plane also has a symmetry condition for the energy equation.

For the height variation, the grid contains 211,200 cells arranged as follows: 100 cells in the x (longitudinal) direction, 44 cells in the y (vertical) direction, and 48 cells in the z (horizontal) direction. The physical dimensions of the baseline grid are about $135D_j$ long, $29D_j$ high, and $40D_j$ wide. The

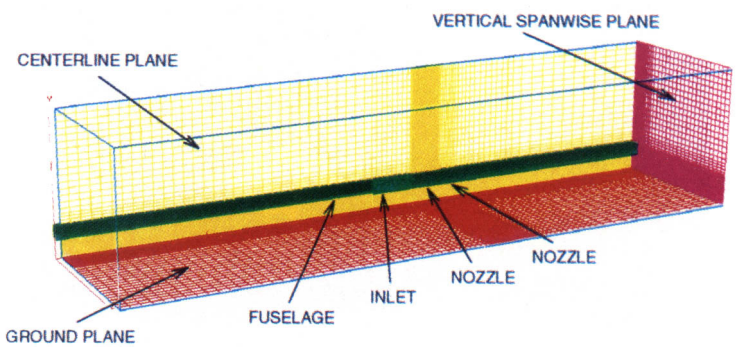

Fig. 3 Grid for baseline case.

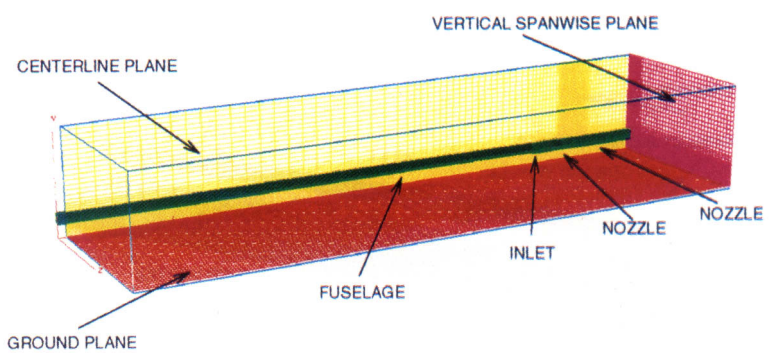

Fig. 4 Grid for head wind speed variation.

aircraft to ground distance was varied by elongating the cells underneath the aircraft. This facilitated the comparative analysis.

The head wind speed variation used a slightly modified grid; 100 cells in x, 44 cells in y, and 60 cells in z, yielding 264,000 total cells (see Fig. 4). This grid has a greater length ($177D_j$) and greater width ($59D_j$) than the baseline grid. Also, the distance in front of the forward pair of jets is greater ($152D_j$ vs $76D_j$ for the baseline grid) to accommodate the long region of hot gas in front of the inlet in the $U_\infty = 0.01V_j$ case. (In each of the grids, the inflow boundary condition is far enough from the stagnation point of the hot ground flow to prevent interference with the fluid mechanics. Also, the tunnel wall boundaries are sufficiently far from the aircraft model to minimize effects on the flowfield.) No grid modification was needed to vary the head wind speed.

Flow Solver

The flowfield in this domain was calculated with a Navier-Stokes, Reynolds-averaged CFD code. References 5–7 describe this steady-state CFD code (and its techniques) for the three-dimensional analysis of turbulent elliptic flows in a Cartesian coordinate system.

The CFD code (CART3D) solves the time-averaged Navier-Stokes or Reynolds equations. The k-ε turbulence model provides closure. The governing equations include continuity, x-, y-, and z-momenta, energy, turbulent kinetic energy, and turbulent energy dissipation. These equations are solved using a block-implicit multigrid algorithm developed by Vanka.[5]

CART3D uses a hybrid-differencing scheme on a staggered grid. This means that the code uses central differencing or upwind differencing, depending upon the cell's Reynolds number. Also, the scalar properties (density, pressure, etc.) are calculated at the cell volume centers, while the velocities are solved at the centers of the cell faces.

The multigrid technique speeds convergence by solving the equations on sequential grids of different cell densities. The flow is initialized on the coarsest grid which gets refined by the multigridding. Dividing each cell on a grid into eight equal cells refines the grid for the next grid level. A V cycle of sweeps on the various grid levels is performed until the solution converges on the finest grid. This technique speeds convergence by dampening out errors with the various levels of grid refinement.

To determine convergence, the residuals are nondimensionalized by an appropriate number, and then the maximum of all the residuals is compared to the tolerance criterion. The tolerance criterion used by this study is 1% for the finest grid. All test cases used the third grid level for the finest grid.

Flowfield Features

A short study of the features in the baseline case will help bring out the differences caused by varying the aircraft altitude, the head wind speed, and the thrust splay angle.

Figure 5 displays the temperature contours in an x-z plane near the ground. These contours show the locations of the forward vortex pair and the two ground vortices generated by the interaction of the jets and the crossflow. The axis for the forward vortex pair is perpendicular to the plane shown in Fig. 5, while the axes for the ground vortices are parallel to the plane. The forward vortex pair is smeared by the steady-state calculations, but still agrees well with the time-averaged experimental data.[8–10]

The particle traces in Fig. 6 reveal ingestion of exhaust gases. The particle traces from the jet region show the forward vortex and ingestion into the inlet. The particle traces starting at the inflow boundary show the head wind's deflection around the forward vortex. Temperature contours along the ground plane are also shown for clarity of position.

Figure 7 shows a three-dimensional temperature contour for the baseline case. This isotherm is for 325 K (125°F), a reasonable upper limit on the temperature of the air reaching the engine. With the ambient flow at 300 K (81°F), this represents a temperature rise of more than 25 K (45°F) for the fluid inside the isotherm. The inlet is almost completely obscured by the contour. Clearly, the engine is exposed to a considerable amount of hot gas from the engine exhaust. The

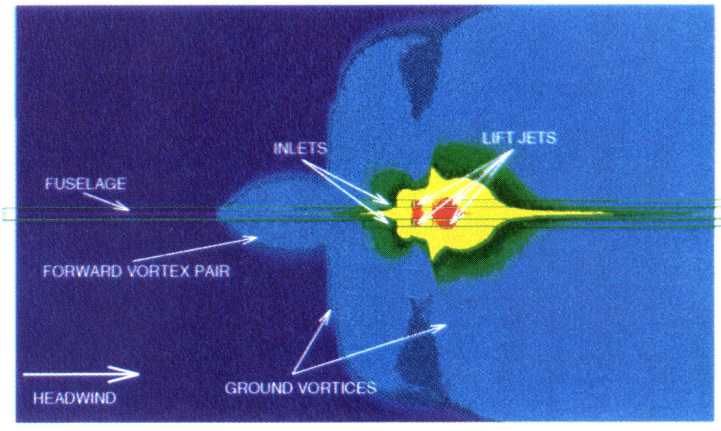

Fig. 5 x-z plane temperature contours $H = 4D_j$, $U_\infty = 0.03V_j$.

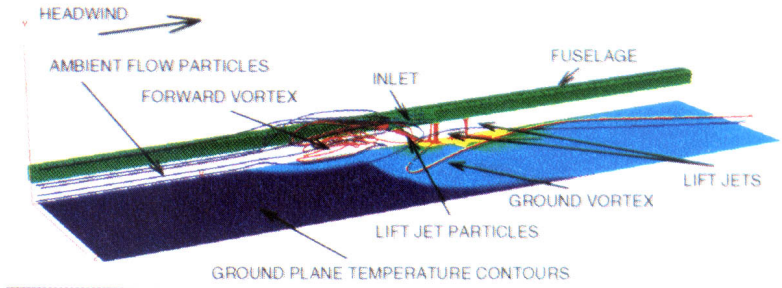

Fig. 6 Select particle traces $H = 4D_j$, $U_\infty = 0.03V_j$.

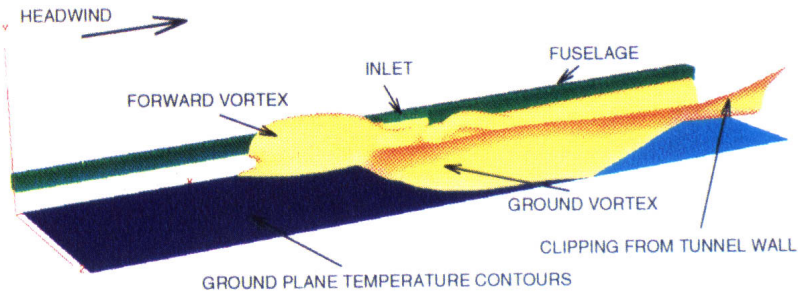

Fig. 7 Three-dimensional isotherm (T = 325 K) $H = 4D_j$, $U_\infty = 0.03V_j$, T_∞ = 300 K, T_j = 1000 K.

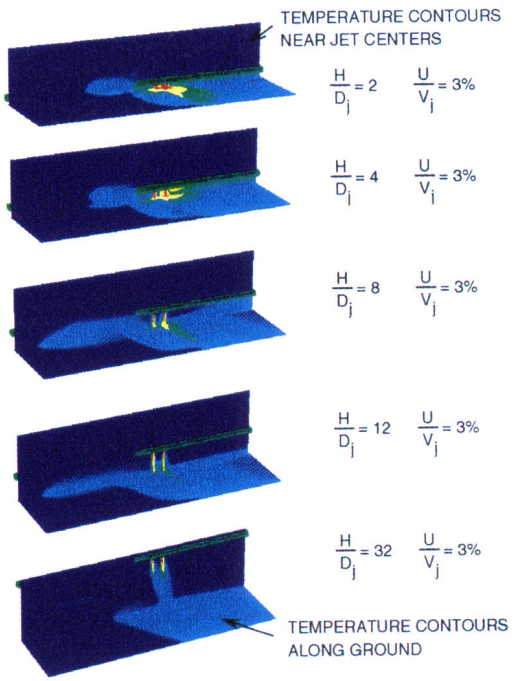

Fig. 8 Temperature contours in select planes ($U_\infty = 0.03V_j$).

bubble in front of the inlet reveals the location of the forward vortex. Note that the clipping of the isotherm in the right side of Fig. 7 is due to wall effects which have no consequence on the hot gas ingestion.

Aircraft Altitude Parameter Variation

The aircraft altitude varied from 2 to $32D_j$. The cases actually computed over this range (H = 2, 3, 4, 5, 6, 8, 12, 16, 24, and $32D_j$) were carefully chosen to capture the changes in the flowfield features. Figure 8 shows temperature contours for select aircraft altitudes (2, 4, 8, 12, and $32D_j$) in two planes: 1) the ground plane and 2) a vertical plane passing through the jets near the jet centers. These cases show the changes in the flowfield affecting hot gas ingestion over the range of variation. In each case, the fuselage is mostly hidden by the vertical plane of temperature contours. The major effects of aircraft altitude can be seen in this figure: the forward vortex changes in character, the amount of hot gas ingested is reduced, and the ground vortices decrease in size.

In Fig. 9, the temperatures at the cells in front of the mass sink or "engine face" are plotted against the aircraft altitude. The temperatures shown are the minimum, the maximum, and a weighted average based on the cell volumes. The spread of the minimum and maximum temperature shows the temperature distortion at the engine face. This, and the average temperature rise above ambient, is plotted in Fig. 10. At low altitudes, the distortion is obviously extreme, and it quickly diminishes with increasing altitude. The average temperature shows a similar behavior. The nonmonotonic behavior at $H = 3D_j$ in all of these curves appears to be physical. At this time, the physical mechanism creating the local increase at H

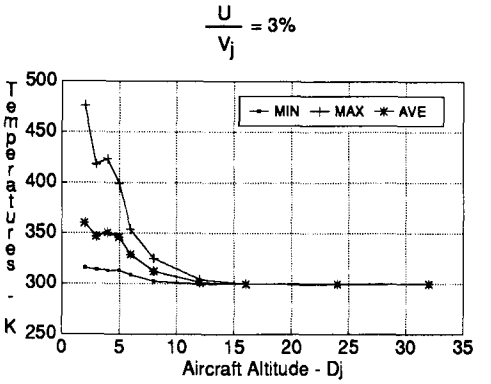

Fig. 9 Plot of engine face temperatures vs aircraft altitude.

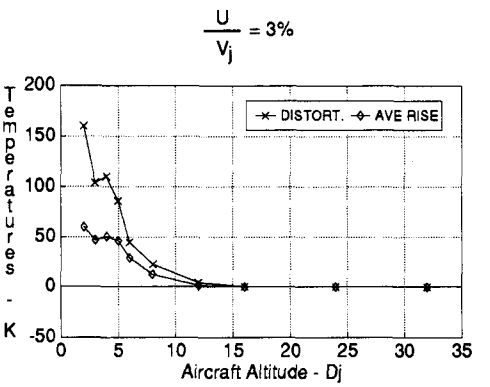

Fig. 10 Distortion and average rise vs aircraft altitude.

$= 3D_j$ is unknown. In tests for grid dependencies, other calculations on different grids exhibited the same trends, including the nonmonotonicity.

Head Wind Speed Parameter Variation

The head wind speed was varied from 1 to 9% of the jet velocity ($U_\infty = 0.01$–$0.09V_j$) in 1% increments for a constant altitude ($H = 4D_j$). Figure 11 displays temperature contours in the same two planes as in Fig. 8; the ground plane and a vertical plane passing through the jets near the jet centers. Selected head wind speeds (1, 3, 5, 7, and 9%) show the changes in the flowfield for the varying head wind speed. Again, the fuselage is mostly hidden by the vertical plane of temperature contours. In Fig. 11 the calculated domain includes a much larger region in front of the inlet in comparison with Fig. 8. This is due to a very long region of exhaust gas which extends in front of the inlet along the ground in the $U_\infty = 0.01V_j$ case.

The effect of head wind speed on the engine face temperatures can be seen in Fig. 12. Note that the minimum temperature declines rather steadily with increasing head wind speed. The general flatness of the average temperature would indicate that near-field ingestion dominates over most of the speed range. The temperature distortion at the engine face varies weakly with head wind speed at the low speeds, and is

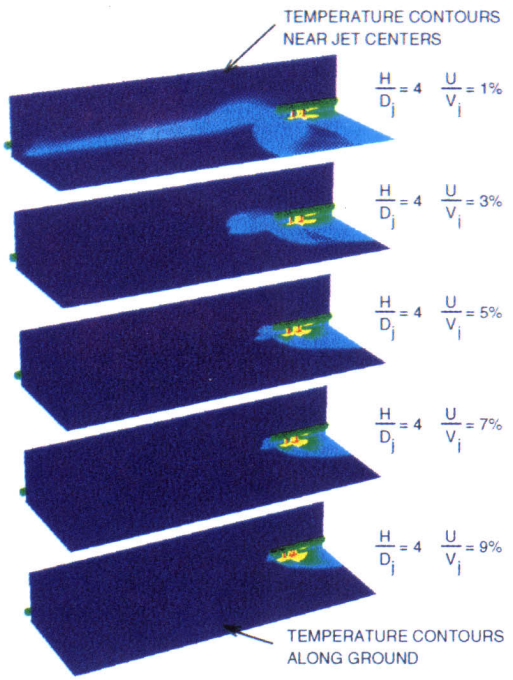

Fig. 11 Temperature contours in select planes ($H = 4D_j$).

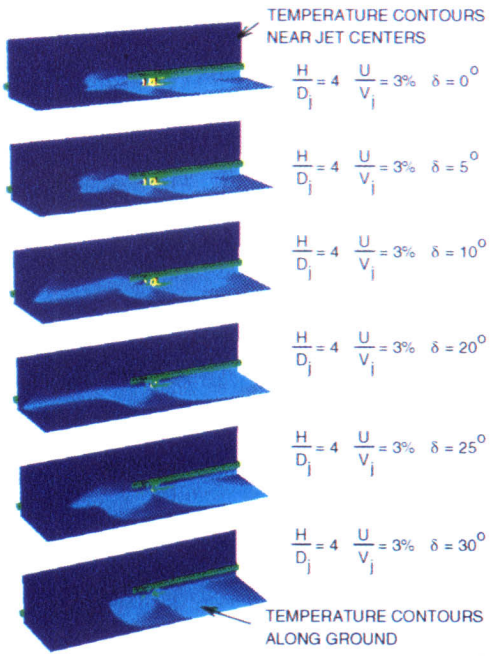

Fig. 14 Temperature contours in select planes—splaying all jets ($H = 4D_j$, $U_\infty = 0.03V_j$).

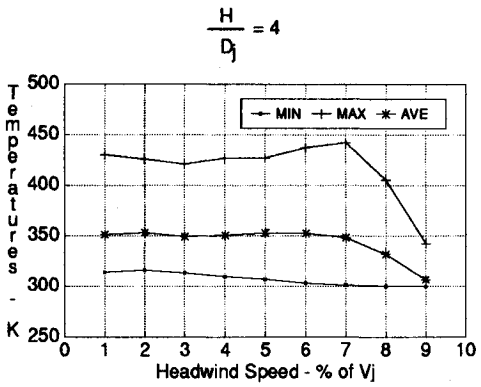

Fig. 12 Plot of engine face temperatures vs head wind speed.

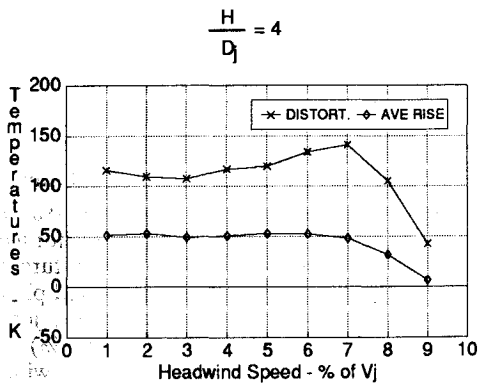

Fig. 13 Distortion and average rise vs head wind speed.

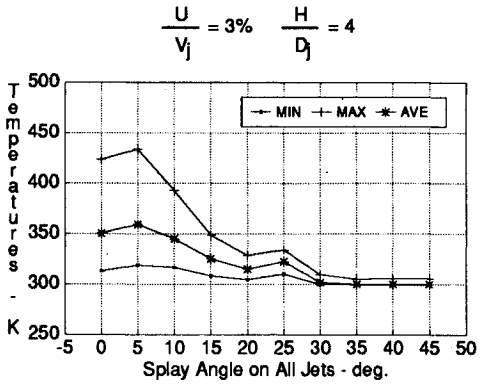

Fig. 15 Plot of engine face temperatures vs splay angle on all jets.

greatest for the 7% case as shown in Fig. 13. One should note that these high-velocity ratios are unrealistically representing a windy vertical landing, but they might be relevant for a low-speed runway landing. For choked jets, the 9% head wind represents about a 110-kt head wind which would either be a hurricane or a slower than normal landing speed for a conventional fighter aircraft.

Thrust Splay Angle Parameter Variation

A technique used to help control hot gas ingestion is to splay the jets. By angling the lift jets, the relative strengths of the fountain, upwash, and vortices are changed, therefore changing the flow structures affecting ingestion. In this study, the splay angle (δ) of the thrust is measured from the downward vertical inward to the centerline plane of the aircraft model. To vary the thrust splay angle, the component velocities on the jets changed to provide the required angle while keeping the speed of the jet constant. Thus, the direction of the lift jets changed while the geometry of the aircraft model did not.

Splaying All Jets

For the first variation of the thrust splay angle, all four jets were splayed the same amount. The splay angle varied from 0 to 45 deg (δ = 0–45 deg) in 5-deg increments for a constant height ($H = 4D_j$) and constant head wind speed ($U_\infty = 0.03V_j$). Figure 14 shows temperature contours in two planes similar to those displayed in Figs. 8 and 11; the ground plane and a vertical plane that is now on the inner side of the lift jets (instead of near the center). Selected splay angles (0, 5, 10, 20, 25, and 30 deg) show the changes in the flow structures due to varying the angle of all the jets. The most noticeable change occurs in the length of the hot gas region in front of the inlet. A less noticeable change is the increase of hot gas directly in front of the inlet for the 5-deg case. This actually causes an increase in hot gas ingestion over the 0-deg case, instead of reducing it.

This and other effects of thrust splay angle for all the jets can be seen in Figs. 15 and 16. In Fig. 15, the average tem-

perature first rises and then drops until a splay angle of about 20 deg, where it starts rising again. A local maximum exists at the 25-deg point before the average temperature flattens out at its lowest value. Both the minimum and maximum temperatures follow the same behavior. The distortion and average temperature rise displayed in Fig. 16 show the same patterns. Note that for this configuration of model and altitude, the jets will converge at the ground for a thrust splay angle of 22 deg.

Splaying Forward Jets Only

In the second variation, only the forward jets varied in thrust splay angle. The rear lift jets maintained a 0-deg splay angle. Again, the thrust splay angle varied from 0 to 45 deg (δ = 0–45 deg) in 5-deg increments at the same altitude ($H = 4D_j$) and head wind speed ($U_\infty = 0.03V_j$), just as in the all jets splayed variation. The calculated results are extremely similar to the results from splaying all the jets. As a matter of fact, a plot of the temperature contours in the same two planes as in Fig. 14 would appear almost identical to Fig. 14

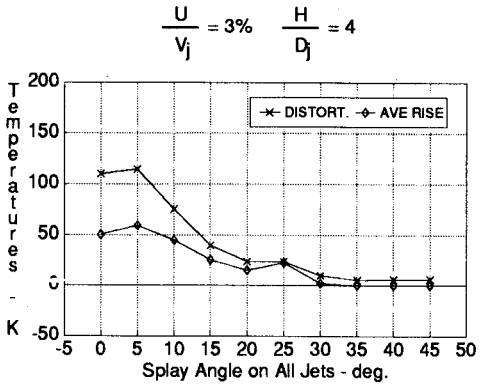

Fig. 16 Distortion and average rise vs splay angle on all jets.

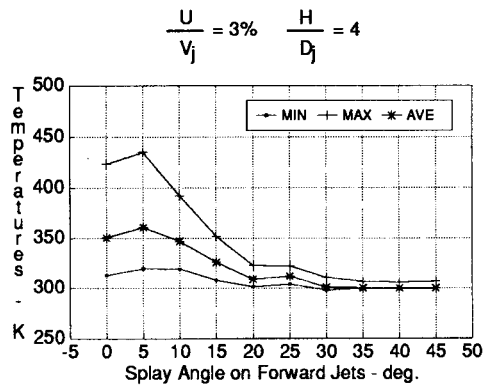

Fig. 17 Plot of engine face temperatures vs splay angle on forward jets.

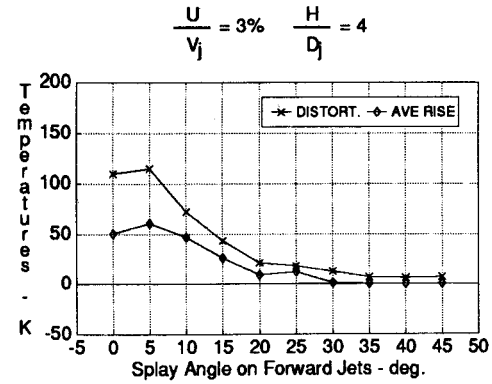

Fig. 18 Distortion and average rise vs splay angle on forward jets.

forward of the jets. (Such a plot does exist in the paper, but it is not here for brevity.)

The ingestion effects of thrust splay angle for the forward jets can be seen in Fig. 17. The average temperature first rises and then drops until a splay angle of about 20 deg, where it rises very slightly. A local maximum exists at 25-deg splay angle before the average temperature drops and flattens out at its lowest value. Both the minimum and maximum temperatures follow a similar behavior. The distortion and average temperature rise displayed in Fig. 18 show the same patterns, just as when all the jets are splayed. Overall, splaying the forward jets alone gives the same effects on hot gas ingestion as splaying all the jets.

Conclusions and Remarks

In summary, the average of the engine face temperatures decreases with increasing height, but is relatively unaffected by head wind speed. Engine face temperature distortion also decreases with increasing height, but increases with head wind speed until the forward vortex is behind the inlet face. The head wind speed variation reveals that (for a constant height) the engine face temperature is dominated by near-field ingestion effects.

As for the thrust splay angle variation, splaying the jets inward (for a constant height and head wind speed) first causes a rise and then a rapid decrease in hot gas ingestion, although a local maximum exists when the jets converge at the ground plane. Also, splaying the forward jets alone, instead of all the jets, gives almost the same reduction in hot gas ingestion without as large a thrust penalty.

A comparison of the $H = 4D_j$, $U = 0.03V_j$ cases in the height parameter variation and the head wind speed parameter variation show the effects of the calculation domain on the flowfield. The vertical walls of the narrower calculation domain definitely affect the ground vortices, but no differences exist in the temperatures reaching the engine. If the overall flowfield is of primary interest, then the tunnel walls would have to be farther from the aircraft model.

This study did not address the importance of the aircraft geometry (fuselage, wings, tails, etc.) in relation to the flowfield. Only one aircraft model was used, and it was quite simplistic.

The last conclusion from this study concerns the practicality of using an efficient CFD code for parameter variation studies. The turnaround time on a Cray-2 supercomputer and state-of-the-art workstations allows quick parameter changes. Typically, a Cray-2 supercomputer solved the flowfield in about an hour with a turnaround time of a day. A dedicated IBM RS-6000 workstation can solve the flowfield in about 6 h and can actually give shorter turnaround than the shared supercomputer.

References

[1]Kuhn, R. E., "Design Concepts for Minimizing Hot-Gas Ingestion in V/STOL Aircraft," *Journal of Aircraft*, Vol. 19, No. 10, 1982, pp. 845–850.

[2]Kuhn, R. E., and Eshelman, J., "Ground Effects on V/STOL and STOL Aircraft—A Survey," AIAA Paper 85-4033, Oct. 1985; see also NASA TM-86825, Nov. 1985.

[3]VanOverbeke, T. J., and Holdeman, J. D., "A Numerical Study of the Hot Gas Environment Around a STOVL Aircraft in Ground Proximity," AIAA Paper 88-2882, July 1988; see also NASA TM-100895, July 1988.

[4]VanOverbeke, T. J., and Holdeman, J. D., "Three-Dimensional Turbulent Flow Code Calculations of Hot Gas Ingestion," *Journal of Aircraft*, Vol. 27, No. 7, 1990, pp. 577–582.

[5]Vanka, S. P., "Block-Implicit Multigrid Solution of Navier-Stokes Equations in Primitive Variables," *Journal of Computational Physics*, Vol. 65, July 1986, pp. 138–158.

[6]Claus, R. W., and Vanka, S. P., "Multigrid Calculations of a Jet in Crossflow," *Journal of Propulsion and Power*, Vol. 8, No. 2, 1992,

pp. 425–431.

[7]Tafti, D. K., and Vanka, S. P., "Hot Gas Environment Around STOVL Aircraft in Ground Proximity—Part 2: Numerical Study," *Journal of Aircraft*, Vol. 29, No. 1, 1992, pp. 20–27; see also AIAA Paper 90-2270, July 1990.

[8]McLean, R., Sullivan, J., and Murthy, S. N. B., "Hot Gas Environment Around STOVL Aircraft in Ground Proximity—Part 1: Experimental Study," *Journal of Aircraft*, Vol. 29, No. 1, 1992, pp. 67–72; see also AIAA Paper 90-2269, July 1990.

[9]McLean, R. J., "The Flowfield Around a STOVL Aircraft Model in Ground Effect," NASA CR-187091, May 1991.

[10]Johns, A. L., Neiner, G., and Bencic, T. J., "Hot Gas Ingestion Test Results of a Two-Poster Vectored Thrust Concept with Flow Visualization in the NASA Lewis 9- by 15-Foot Low Speed Wind Tunnel," AIAA Paper 90-2268, July 1990; see also NASA TM-103258, July 1990.